



44 dispersion by CNF is responsible for this enhancement. The study highlights the use of  
45 biodegradable nanocellulose for the preparation of sustainable PCM composites with improved  
46 performance. These PCM composites are scalable, they have potential to increase energy  
47 efficiency and revolutionize the heating/cooling applications in buildings and other TES systems.

48 **Keywords:** Thermal energy storage, supercooling, calcium chloride hexahydrate, cellulose  
49 nanofibril, graphene nanoplatelets, thermal conductivity

## 50 1 Introduction

51 Global energy consumption rates continue to increase due to a growing population, expanding  
52 economy, and a rising desire for a better quality of life [1]. The major contribution to energy  
53 consumption comes from heating and cooling of residential and commercial buildings that  
54 contributes to 40% of total annual electricity consumption. Due to the widespread usage of fossil  
55 fuels and greenhouse gas emissions, the increased energy consumption will have a negative impact  
56 on the global energy ecosystem. Therefore, it is imperative to develop eco-friendly, renewable,  
57 and sustainable energy generation and storage solutions for building technology applications.  
58 Utilizing latent heat thermal energy storage systems (LHTESS) is a suitable and efficient strategy  
59 for storing energy for use at a later time, leading to increased energy efficiency and cost savings  
60 [2]. Phase change materials (PCMs), a notable class of LHTESS, have attracted interest due to  
61 their remarkable thermophysical properties [3]. These materials have a variety of uses, including  
62 buildings [4], cooling [5], desalination [6], and heat exchangers [7]. In building applications,  
63 PCMs are utilized to minimize heat transfer between a building and its environment. PCMs store  
64 energy in both sensible and latent forms, allowing them to minimize heat transfer between a  
65 building and its environment [8].

66 Inorganic PCMs based on salt hydrates for latent heat thermal energy storage are a prominent  
67 subset of PCMs that attracted considerable attention, due to their high volumetric energy storage  
68 capacity, availability across a broad range of acceptable melting temperatures, non-flammability,  
69 significant volumetric storage capacity, and cost-competitiveness relative to other PCM classes  
70 such as paraffin, waxes, and fatty acids [9]. While pure salt hydrates like sodium sulfate  
71 decahydrate ( $\text{Na}_2\text{SO}_4 \cdot 10\text{H}_2\text{O}$ ) and calcium chloride hexahydrate ( $\text{CaCl}_2 \cdot 6\text{H}_2\text{O}$ , CCH) may meet  
72 the temperature and energy storage capacity requirements for building applications, they also  
73 suffer from limitations due to incongruent melting, phase separation, low thermal conductivity,  
74 and supercooling [10,11]. When phase separation occurs, there is a high likelihood of precipitation  
75 of anhydrous salt or partial hydrates during the melting of salt hydrates, attributed to the difference  
76 in solubility. The settling of the salt ultimately leads to a drop in the energy storage capacity of the  
77 PCM after successive thermal cycles [11]. Also, supercooling phenomenon results in crystallizing  
78 at temperatures substantially below the freezing temperature due to the absence of adequate  
79 nucleation sites to trigger crystallization. This impacts the release of heat by salt hydrates and  
80 causes a large temperature differential between melting and freezing. Therefore, to realize the  
81 promise of PCMs for widespread TES applications, these fundamental issues must be addressed.

82 To address the critical challenges in salt hydrate PCMs, several approaches are utilized including  
83 the use of additives such as thickeners, thermally conductive fillers, and nucleators to withstand  
84 numerous heat cycles, increase thermal conductivity and reduce supercooling effectively [5,10,12–  
85 14]. For instance, Zhang et al. [15] fabricated a composite PCM based on CCH, diatomite, and  
86 paraffin. The enthalpies of fusion and freezing for the resultant composite are 108.2 and 98.5  $\text{Jg}^{-1}$ ,

87 respectively. The composite showed excellent stability up to 100 melt-freeze cycles. By combining  
88 urea, ammonium chloride, and SCH with sodium carboxymethyl cellulose as nucleators, Li et al  
89 [16] were able to adapt and optimize the characteristics of CCH. The final PCM composite has the  
90 following properties: 9.51 °C phase change temperature, 0.39 °C supercooling degree, 99.08 Jg<sup>-1</sup>  
91 melting enthalpy, and 0.330 W/m-K thermal conductivity. The PCM showed good thermal  
92 reliability and stability after 50 successive thermal cycles. In another work, Thakkar et al. [17]  
93 reported a CCH-based composite PCM with optimized thermal properties using 2 wt% of SCH to  
94 reduce supercooling from 12 °C to 0 °C. Furthermore, 5 wt% NaCl/KCl was utilized as a stabilizer,  
95 preventing phase separation and incongruent melting. The prepared composite PCM had a melting  
96 enthalpy of 169 Jg<sup>-1</sup> after 25 melt-freeze cycles. The supercooling degree of CCH was found to be  
97 decreased from 22.06 °C to 3.89 °C when using 1 wt% boron nitride nanosheets, as reported by  
98 Zhang et al. [18]. The thermal conductivity also rose, from 0.3 to 3.918 W/m-K. During further  
99 investigation, it was found that after 20 cycles, the latent heat of melting was 144.19 Jg<sup>-1</sup>. In another  
100 study, Xu et al. [19] reported a novel composite PCM using CCH with graphene oxide nano-sheets  
101 and SCH. The novel PCM significantly reduced supercooling degree in CCH by 99.2% and the  
102 reported melting enthalpy was 198.20 Jg<sup>-1</sup> after 250 cycles. While these studies have shown  
103 property enhancement of CCH salt hydrates using various additives, some additives require harsh  
104 conditions of increased temperature or acidic treatment during preparation and expensive materials  
105 cost, for example boron nitride nanosheets, and graphene oxide. Moreover, there is a sparse  
106 knowledge on the impact of the thickeners and additives on the rheological properties of the salt  
107 hydrate. Thus, there is a need for further research on the adoption of environmentally friendly  
108 additives to enhance the properties of salt hydrates for better design efficient PCM.

109 Nanocellulose-based materials including cellulose nanofiber (CNF) have recently gained research  
110 attention for the enhancement of salt hydrate PCMs due to their excellent chemical and thermal  
111 stability, sustainability, high abundance, as well as low cost [20–22]. CNFs have high moduli and  
112 aspect ratio, which enhances the formation of entangled networks with high gel strength when  
113 dispersed in an aqueous medium [23]. The gel strength is dependent on the concentration of CNF  
114 added to the mixture, as reflected by the storage and loss moduli values. At the critical  
115 concentration of CNF, the mixture forms a three-dimensional gel-like structure due to the  
116 entanglement of the nanofibrils and the hydrogen bonds between adjacent nanofibrils, which could  
117 form a compact structure in PCM mixtures [24]. Also, there is an increase in viscosity by physical  
118 thickening which limits the diffusion length of water and helps prevent phase separation or  
119 incongruent melting in salt hydrates. To enhance the thermal conductivity of salt hydrates, carbon-  
120 based materials including graphene, expanded graphite (EG), carbon nanotube (CNT), graphene  
121 oxide (GO), and graphene nanoplatelet (GNP) have been used extensively [25–28]. This is due to  
122 their high thermal conductivity. For instance, Hirschey et al [29] reported a 583% increase in  
123 thermal conductivity of salt hydrate PCM mixture when 25wt% EG was introduced. Shen et al.  
124 [24] also used GNP as thermal conductivity enhancers for sodium acetate trihydrate based PCMs  
125 and 55.2% increased in thermal conductivity was achieved with 2.5wt% GNP. However, these  
126 carbon-based thermal conductivity enhancers are prone to aggregation due to the influence of van  
127 der Waals interaction among the particles [24,30]. To solve the agglomeration problem with  
128 carbon-based thermal conductivity enhancers, this study shows that CNF could be adopted as an  
129 excellent dispersant of the carbon-based thermal conductivity enhancer in the PCM systems,  
130 thereby improving the overall properties of the composite PCMs. This is justified with other  
131 studies reporting that CNF has been demonstrated to effectively disperse these carbon-based  
132 components without affecting their characteristics [31–33].

133 Therefore in this work, we investigated the enhancement of CCH PCM by reducing supercooling,  
 134 improving thermal energy storage performance and thermal conductivity by leveraging the  
 135 synergistic effect of CNF and nano-based additives. First, biodegradable CNF was incorporated  
 136 with CCH to develop CNF-based PCM composites with enhanced thermal energy storage  
 137 performance. Rheological experiments were used to examine the impact of thickening and  
 138 different concentration of CNF that provides the highest stabilization in CCH. Furthermore, the  
 139 right range of concentration of the nucleating agent was analyzed to give the lowest degree of  
 140 supercooling in CCH. GNP was added to improve the thermal conductivity of the composite  
 141 material. The produced PCM composites were thoroughly analyzed to characterize their structure,  
 142 morphology, thermal properties, and thermal cycling stability. Also, the enhancement mechanism  
 143 of the PCM was explained. The amphiphilicity of CNF is a key factor in the dispersion of GNP in  
 144 the PCM composite, leading to the formation of a compact and stable PCM composite with  
 145 enhanced thermal properties. The prepared PCM composites could be integrated into the TES  
 146 system for residential and commercial building applications.

## 147 2 Materials and Methods

### 148 2.1 Materials

149 Calcium chloride hexahydrate ( $\text{CaCl}_2 \cdot 6\text{H}_2\text{O}$ , CCH, purity  $\geq 99\%$ ), and strontium chloride  
 150 hexahydrate ( $\text{SrCl}_2 \cdot 6\text{H}_2\text{O}$ , SCH, purity  $\geq 99\%$ ) were obtained from Sigma-Aldrich, cellulose  
 151 nanofibril (CNF) were from University of Maine Process Development Center, and XG Sciences  
 152 Inc. supplied graphene nanoplatelets (GNP, Grade M) with a mean particle size of 5 nm. Materials  
 153 were used as-is, without any further treatment. The thermophysical properties of the materials used  
 154 in this study are reported in the Table 1 below:  
 155

156 **Table 1. Properties of materials used in this study**

157

Material*	Melting point ( $^{\circ}\text{C}$ )	Particle size (nm)	Thermal conductivity (W/m.K)	
			Solid	Liquid
$\text{CaCl}_2 \cdot 6\text{H}_2\text{O}$ (CCH) <sup>a</sup>	29.8	-	1.0	0.54
$\text{SrCl}_2 \cdot 6\text{H}_2\text{O}$ (SCH)	115	-	-	-
Graphene nanoplatelet (GNP)	3652-3697	5 – 15	3000 <sup>b</sup>	-
Cellulose nanofiber (CNF)	-	5 – 200	-	-

158 \*Thermophysical properties are obtained from the materials safety data sheet

159 <sup>a</sup> Melting enthalpy is 190 J/g

160 <sup>a</sup> Thermal conductivity value when considered parallel to the surface

161

### 162 2.2 Methodology

#### 163 2.2.1 Preparation of CCH/SCH, CCH/CNF, and CCH/SCH/CNF mixtures

164 Using CCH as the main component, CCH/SCH mixture was prepared by heat mixing CCH and  
 165 SCH for 1 hour in a 50  $^{\circ}\text{C}$  ultrasonification bath to enable homogenous mixing. In all formulations,  
 166 the amount of CCH was fixed while SCH was added with variation in doses between 1-7 wt%.  
 167 The CCH/SCH mixtures were labelled as CCH-S<sub>1</sub>, CCH-S<sub>3</sub>, CCH-S<sub>5</sub>, and CCH-S<sub>7</sub>. CCH/CNF  
 168 mixtures were prepared by mixing various concentrations of CNF from 0.5 wt% - 2 wt% with a

169 fixed concentration of CCH and stirring the mixture magnetically for 50 °C to ensure homogeneity.  
 170 For the preparation of CCH/SCH/CNF mixtures, several doses of CNF ranging from 0.5 wt% - 2  
 171 wt% was added to a fixed concentration of CCH and SCH. Further, the PCM mixtures were  
 172 magnetically stirred for 1 hour at 50 °C to enable a uniform mixture. The obtained mixtures were  
 173 labelled as CCH-SC<sub>0.5</sub>, CCH-SC<sub>1.0</sub>, CCH-SC<sub>1.5</sub>, and CCH-SC<sub>2.0</sub>.

### 174 2.2.2 Preparation of nano-PCM composites

175 To prepare the nano-PCM composite, CCH, SCH, CNF, and GNP were mixed and kept under  
 176 magnetic stirring for 1 hour in a 50 °C water bath to enable homogenous mixing and dispersion.  
 177 After thorough homogenization, the prepared composite PCM was allowed to cool to room  
 178 temperature before further characterization. It is important to note that the GNP was used as  
 179 received without further processing and the CCH, SCH, and CNF components were kept at a fixed  
 180 concentration while varying the dosage of nanoadditive, GNP from 1wt% to 2wt%. The prepared  
 181 nano-PCM composites were labelled as CCH-SCG<sub>1.0</sub> and CCH-SCG<sub>2.0</sub>. Furthermore, the sample  
 182 matrix of the various formulations of the composite PCMs is reported in Table 2.

183 **Table 2.** The compositions of composite PCMs containing CCH, SCH, CNF, and GNP

Sample ID	wt% of SCH, CNF, and GNP added to 100wt% of CaCl <sub>2</sub> .6H <sub>2</sub> O		
	SCH (wt%)	CNF (wt%)	GNP (wt%)
CCH-S <sub>1</sub>	1	0	0
CCH-S <sub>3</sub>	3	0	0
CCH-S <sub>5</sub>	5	0	0
CCH-S <sub>7</sub>	7	0	0
CCH-C <sub>0.5</sub>	0	0.5	0
CCH-C <sub>1.0</sub>	0	1.0	0
CCH-C <sub>1.5</sub>	0	1.5	0
CCH-C <sub>2.0</sub>	0	2.0	0
CCH-SC <sub>0.5</sub>	3	0.5	0
CCH-SC <sub>1.0</sub>	3	1.0	0
CCH-SC <sub>1.5</sub>	3	1.5	0
CCH-SC <sub>2.0</sub>	3	2.0	0
CCH-SCG <sub>1.0</sub>	3	1.0	1.0
CCH-SCG <sub>2.0</sub>	3	1.0	2.0

### 184 2.2.3 Sample Characterization

185 The structure of the PCM samples was studied using X-ray diffraction (XRD). The XRD patterns  
 186 of the PCM mixes were collected using a PANalytical Empyrean diffractometer to ascertain the  
 187 crystal structure of the materials. The tube current was 40 mA, and the X-ray voltage was 45 kV;  
 188 the Cu anode had a K $\alpha$  of 1.54 Å. At a scan rate of 1 °/min, XRD data were recorded across a 2 $\theta$   
 189 range of 5 ° to 90 °. Attenuated total reflectance infrared spectroscopy (ATR-IR) spectra were  
 190 obtained using a PerkinElmer Frontier FTIR/NIR spectrometer fitted with a diamond ATR  
 191 attachment with a spectral resolution of 2 cm<sup>-1</sup> in the 600–4000 cm<sup>-1</sup> range to examine the chemical  
 192 structure of the salt hydrate samples.

193 The thermophysical properties of the materials, such as phase change temperature and latent heat,  
 194 were investigated utilizing a differential scanning calorimeter (DSC 2500, TA Instruments) under

195 a 50 mL/min nitrogen purge. Thermal cycling was performed on 10-20 mg of each sample at a  
196 ramp rate of 5 °C/min between -40 and 50 °C in a hermetically sealed aluminum DSC pan. Melting  
197 temperatures and phase transition enthalpies of PCM samples were determined from heating scans  
198 using TA Instruments TRIOS Software.

199 Due to the low sample utilization and the limited capability of DSC characterization to show phase  
200 segregation and supercooling to scale, the thermal cycling stability of PCM samples across a broad  
201 range of temperatures was investigated using the Temperature-History (T-H) method. During the  
202 T-H test, 15-20 g of PCM samples were placed within a borosilicate glass tube (length ~190 mm,  
203 diameter ~10 mm). A 1/16-inch diameter hole for a T-type sheathed thermocouple insert was  
204 molded into the rubber plug that sealed the glass tube. A borosilicate glass tube was filled with  
205 water to serve as a reference medium. The glass tubes were subjected to thermal cycling at a ramp  
206 rate of 5 °C/min between 5 and 50 °C in an ambient temperature chamber (ESPEC SH-242). The  
207 chamber temperature was also measured using a 1/16 inch sheathed type T thermocouple. The  
208 temperature of the chamber, reference, and PCM samples were acquired using a National  
209 Instruments cDAQ 9214 data collecting system at a sampling rate of 1 second per sample. The  
210 temperature profile was used to examine the melting and freezing behavior of PCM samples. The  
211 phase change temperature, latent heat, and supercooling were analyzed in accordance with these  
212 earlier studies [34,35].

213 Using field-emission scanning electron microscopy, the microstructure and morphologies of the  
214 base materials and the composite PCMs were studied. Furthermore, optical microscopy was used  
215 to examine the structures of the CCH-based composites at room temperature. The rheological  
216 characteristics of the PCM were examined using a rotating rheometer (ARES-G2; TA Instruments)  
217 with a 40 mm diameter parallel plate geometry. The PCM samples were sandwiched between the  
218 plates with a 1 mm separation. To prevent the evaporation of water from the samples, a solvent  
219 trap was used. At 40 °C, the viscosity was evaluated as a function of shear rates ranging from 0.1  
220 to 100 s<sup>-1</sup>, and samples were tested in shear rate-controlled mode. The linear viscoelastic area was  
221 confirmed using an amplitude sweep test at a constant angular frequency (1 Hz) and a range of  
222 strain from 0.1% to 1000%. Oscillatory tests were performed on PCM samples by measuring the  
223 storage (G') and loss (G'') moduli as a response to frequency (1-10 Hz) at a constant strain of 1%.  
224 To ensure that the PCM stayed molten during the measurement, we kept the temperature at 50 °C.  
225 Also, the nucleator, SCH was excluded from all the tested samples.

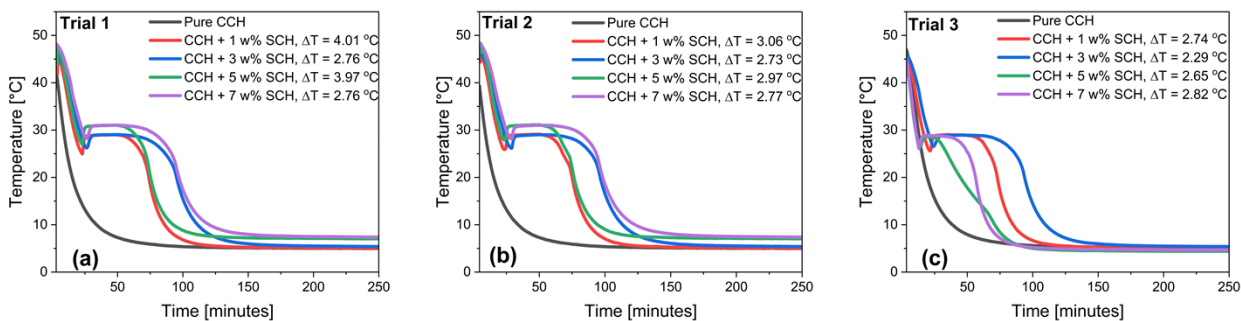
226 The Hot Disk technique [3][4] was used to determine the thermal conductivity of the PCM  
227 samples. This method provides a direct measurement of the samples' thermal conductivity. A  
228 flexible sensor/heater with 2.0–7.5 mm radii and double-spiral nickel wire is inserted in the molten  
229 PCM bulk samples for about 5–20 s at 0.1–1.0 W power. Under constant power, the resistance of  
230 the nickel heater is evaluated. Also, the temperature at the contact may be calculated using the  
231 known temperature coefficient of resistance of nickel. Through analysis of the recorded transient,  
232 the thermal conductivity of the material can be determined. This method is in accordance with ISO  
233 for measuring the thermal conductivity of materials [38].

### 234 **3 Results and Discussion**

#### 235 **3.1 Determination of the concentration ranges of nucleating agent**

236 A major challenge with the use of CCH-based PCM in thermal energy storage applications is the  
237 high degree of supercooling, which causes unpredictable phase change and temperature swings in

238 the material. The degree of supercooling,  $\Delta T$  is defined as the difference between freezing  
 239 temperature ( $T_f$ ) and the onset of nucleation ( $T_n$ ), i.e. ( $\Delta T = T_f - T_n$ ) [14]. As seen in the cooling  
 240 curves of the PCM mixtures after 3 trials using the T-history method in Figure 1, pure CCH did  
 241 not show freezing throughout the period under consideration, owing to higher degree of  
 242 supercooling, in essence there is the absence of adequate nucleation sites to initiate crystallization  
 243 or freezing. A common solution to this challenge is the use of a nucleation agent with a very similar  
 244 crystal structure to CCH and stability above the phase change temperature of CCH [39]. SCH,  
 245 which is isostructural with CCH and has a phase change temperature of 115 °C was selected and  
 246 tested as the potential nucleation agent. The cooling behavior of CCH with different concentrations  
 247 of SCH (1 wt% – 7 wt%) under 3 different trials are shown in Figure 1. The results showed that  
 248 the supercooling of the PCM mixtures drastically decreased to  $\sim 4.0$  °C. This confirms the  
 249 effectiveness of SCH in providing adequate nucleation sites and enabling the timely crystallization  
 250 of CCH. The similar crystal structure of SCH and CCH promotes adherence of CCH to the surface  
 251 of SCH for faster nucleation [19]. In determining the amount of SCH required for effective  
 252 supercooling reduction, the repeated trials revealed that the concentration of SCH at 3 wt% showed  
 253 the lowest degree of supercooling. It is important to note that the supercooling degree varies among  
 254 the samples after repeated trials, this signifies the stochastic nature of the supercooling process.  
 255 Also, the freezing or release of thermal energy by the PCM sample with 3 wt% SCH showed  
 256 outstanding performance among the other concentrations after repeated analyses as revealed by  
 257 the freezing plateau, this indicates that the 3 wt% concentration of SCH is effective for reducing  
 258 supercooling in CCH. This agrees with the study by Li et al. in which 3 wt% of SCH was reported  
 259 as the ideal concentration for favorable reduction of supercooling [10]. Therefore, a 3 wt% SCH  
 260 was used for further testing. Although these experimental results indicate an optimal SCH  
 261 concentration near 3%, the sensitivity of supercooling to the SCH concentration is not significant  
 262 across the range evaluated.  
 263

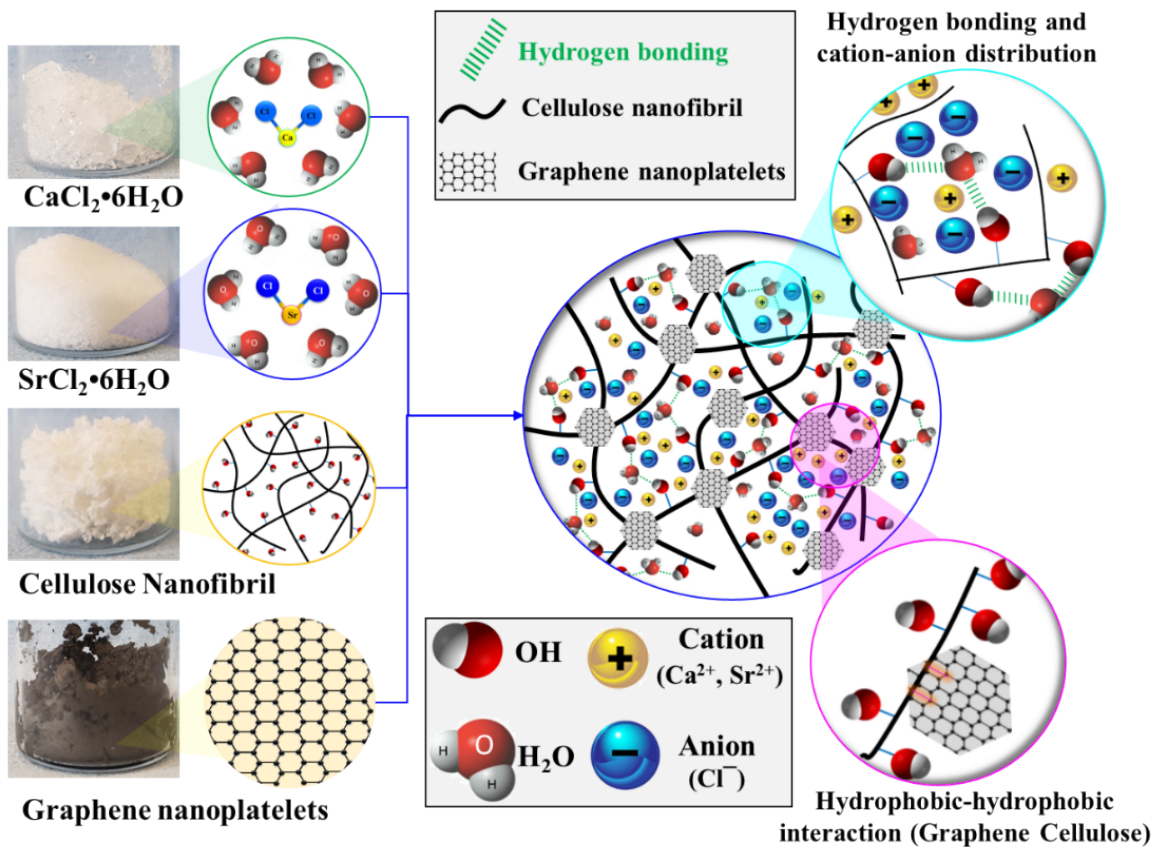


264  
 265 *Figure 1. Cooling curves for CCH with several concentrations of SCH under 3 different trials to*  
 266 *determine supercooling degree.  $\Delta T$  is the difference between freezing temperature and the onset*  
 267 *of nucleation temperature.*  
 268

### 269 3.2 Utilization of CNF and GNP in the synthesis of PCM composites

270 Another limitation that has hindered the widespread adoption of CCH in TES systems is low  
 271 thermal conductivity. This impacts the charging and discharging rate of the salt hydrate thereby  
 272 resulting in protracted thermal cycling duration, and ultimately lower thermal performance [18].  
 273 A solution to this problem includes the use of low-cost, higher thermal conductivity materials as  
 274 additives to enhance the effective conductivity of the CCH mixture. Graphene-based materials find

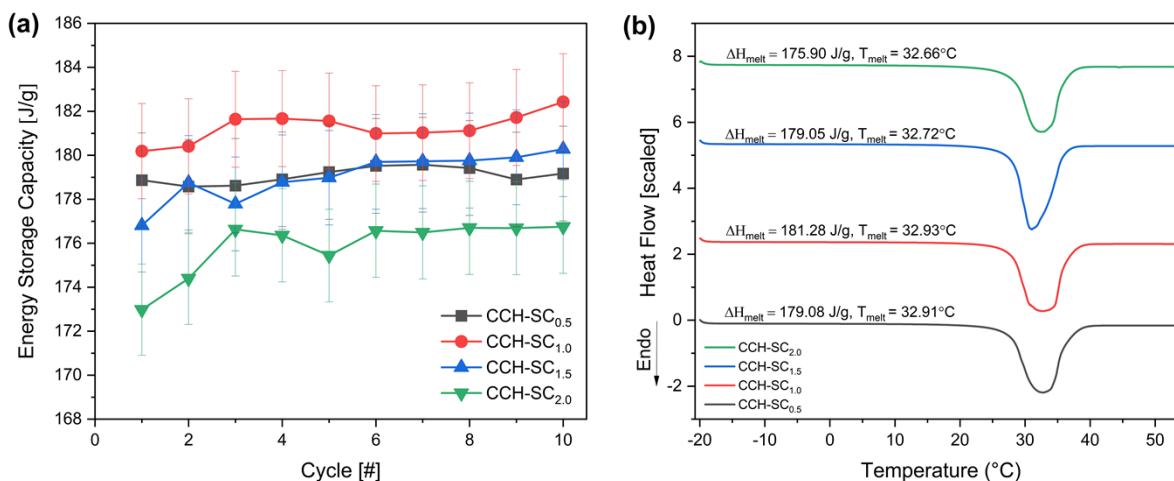
275 relevance in improving the heat-transfer properties and efficiency of PCMs due to their intriguing  
276 thermal characteristics [29]. Graphitic materials including graphene, compressed expanded natural  
277 graphite, and functionalized graphene oxides can be used to improve thermal conductivity.  
278 Although functionalized graphene oxides (GO) have been shown to have superior self-dispersing  
279 capacity relative to graphite and graphene, the severe preparation conditions of these  
280 functionalized GO induce structural defects in these materials which significantly affects their  
281 thermal characteristics [40]. Furthermore, the chemical modification and functionalization of  
282 graphene and graphite to enhance dispersion are also difficult, expensive, and detrimental to the  
283 environment [24]. By using an ecofriendly dispersion procedure of GNP using CNF, we developed  
284 a PCM composite with enhanced thermal properties based on CCH (salt hydrate), CNF  
285 (dispersant), GNP (thermal conductivity enhancer), and SCH (nucleator). A possible explanation  
286 is that the enhancement mechanism relies on CNF's entangled structure and amphiphilicity, which  
287 enable it to engage in hydrophobic contact with GNP, resulting in an increase in the dispersion of  
288 GNP in the composite system [41]. Also, CNF is capable to induce hydrogen bonding in the  
289 material system, thereby controlling the release of water needed for crystallization and preventing  
290 incongruent melting of CCH (Figure 2). Shen et al. [24] reported that GNP concentrations above  
291 2.5 wt% did not show effective dispersion in the PCM matrix, due to the aggregation of the  
292 nanomaterials in the PCM composite. Therefore, the concentration of GNP evaluated in this study  
293 is between 1 wt% – 2 wt% for higher dispersion. To achieve maximum thermal performance of  
294 the PCM composite, it is also important to optimize the ratio of CNF added to the composite  
295 system. To this end, 3 wt% of SCH nucleator, and several concentrations of CNF ranging from 0.5  
296 wt% to 2 wt% were added to CCH. The energy storage capacity of the respective composites was  
297 tested after repeated thermal cycling. As shown in Figure 3, the samples with 0.5wt% - 1.5wt%  
298 CNF have similar melting enthalpy values and sample with 1 wt% CNF showing the highest value  
299 of energy storage capacity of 181 Jg<sup>-1</sup>. Further increase in the concentration of CNF to 2 wt% led  
300 to a corresponding decrease in the latent heat energy of the composites to 175 Jg<sup>-1</sup>. The phase  
301 change temperatures of the composites were measured in the range of 32.66 °C – 32.93 °C (Figure  
302 3b). The addition of CNF led to an increase in the melting point of pure CCH from ~29 °C[42] to  
303 ~32 °C. The presence of fibrous structure of CNF in the PCM mixture delays the bond dissociation  
304 of the atoms in the PCM mixture thereby leading to an increase in the melting point of the PCM  
305 mixture.  
306  
307



308

309 *Figure 2. Schematic showing the interactions of constituents in the PCM composite, enabling a*  
 310 *uniform dispersion of GNP and favorable steric and ionic interactions, contributing to a highly*  
 311 *stable PCM.*

312



313

314 *Figure 3. Thermal properties of CCH-based composite (a) Change in energy storage capacity of*  
 315 *CCH-SC composites in 10 cycles (b) DSC curves of CCH-SC composites.*

316

### 3.3 Microstructure Characterization of the PCM Composites

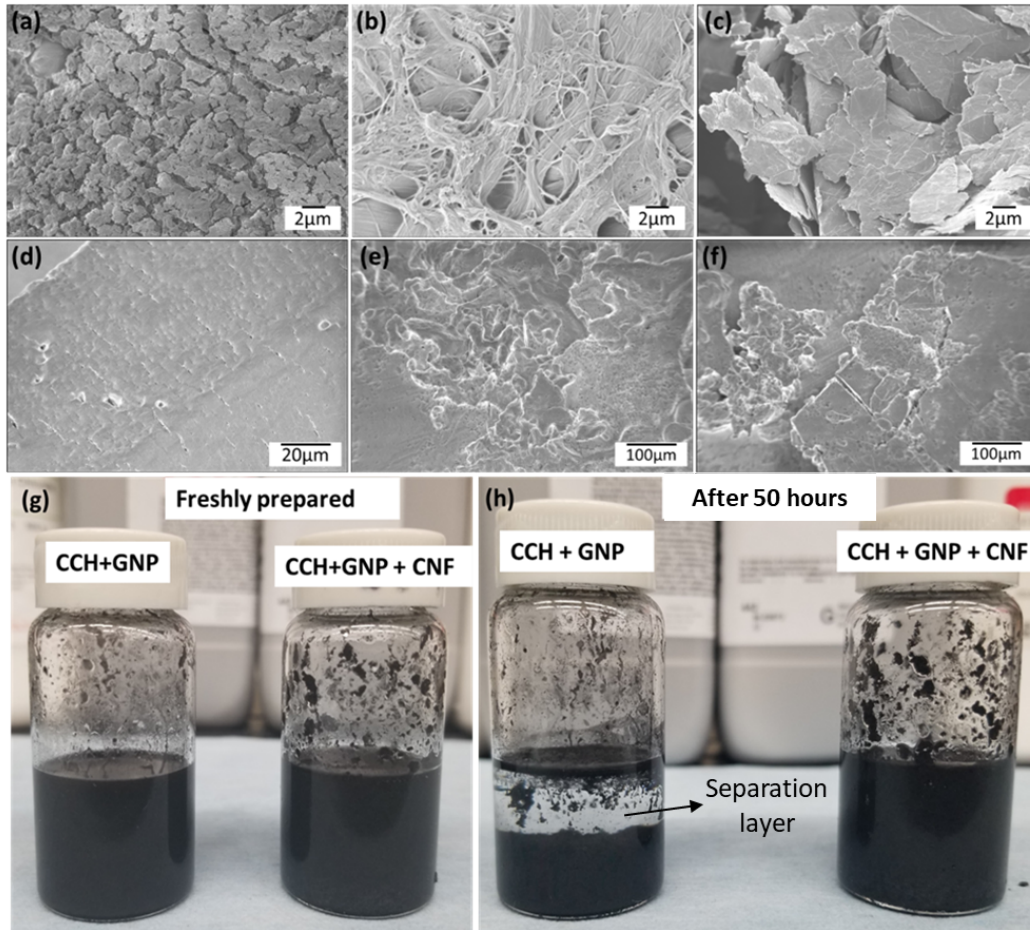
Scanning electron microscopy (SEM) was used to examine the microstructure and morphology of the base materials and PCM composites at room temperature (Figure 4). First, Figure 4a shows the SEM micrograph of pure CCH, which has a coarse crystalline structure and a crystal size estimated to be less than five microns. The micrograph of CNF is characterized by a high aspect ratio and entangled network structure, as shown in Figure 4b. The SEM image of GNP showed a sheet-like structure with uneven multilayers and spaces between them (Figure 4c). With the introduction of SCH and CNF to CCH, the resulting composite showed a compact structure with a smooth appearance throughout the cross-section (Figure 4d). This indicates the compatibility of the base materials to form a homogenous phase. The compact structure of the composite is related to the charge screening effect by the ions of the salt hydrate particles making the cellulose fibrils repel each other less strongly. The change in the colloidal contact coupled with the enhanced hydrogen bonding between the fibrils reinforces the fiber networks and causes the nanocellulose to be denser [41][43]. As a consequence, the PCM composite becomes uniform. Also, the micrograph of PCM composites containing 1 wt% GNP and 2 wt% GNP are displayed in Figure 4e and Figure 4f, respectively. The composite showed a homogenous structure with the fibrillated network of CNF spreading uniformly to enhance the dispersion of GNP throughout the composite matrix. The effective dispersion of GNP is attributed to hydrophobic interactions between GNP and CNF in which the CNF is linked to the GNP sheets. The CNF stabilizes the dispersed GNP by sterically impeding its reaggregation [44]. Hence, the dispersive properties of CNF enabled the formation of PCM composites with homogenous structures. To confirm the dispersive abilities of CNF visually, two CCH and GNP-based samples, with and without CNF were prepared as shown in Figure 4g. After 50 hours, changes in the samples were observed (Figure 4h). In the sample without CNF as the dispersant, GNP particles settled down and agglomerated showing a separation layer. However, the sample with CNF (1wt% CNF) maintained its homogeneity. This further confirms the efficacy of CNF as a promising dispersant aiding the uniform distribution of thermal conductivity additives in PCMs systems.

### 3.4 Rheology of the PCM composites

Rheological tests were conducted on CCH with varying concentrations of CNF (0.5 wt%, 1 wt%, 1.5 wt%, and 2 wt%) at the melted state (40 °C) to evaluate the impact of the thickener on the rheological properties of CCH and to determine the critical concentration of the thickener for enhanced PCM properties; the results of these tests are presented in Figure 5. First, the flow property of the PCMs, which is sensitive to the rate of change in viscosity with strain was evaluated using a flow sweep test as illustrated in Figure 5a. The pure CCH sample shows Newtonian behavior with a relatively constant viscosity of 0.02 Pa·s across a range of shear rates. This behavior is expected since CCH contains a significant quantity of water of crystallization and water behaves as a Newtonian fluid. However, the introduction of CNF changes the flow properties of the PCM from Newtonian behavior to non-Newtonian behavior. In essence, the PCM composites containing CNF showed a shear thinning behavior in which the viscosity of the mixtures reduces as the applied shear rate increases. The viscosity values follow the well-established power law as shown below [45]:

$$\eta = K\gamma^{n-1} \quad (1)$$

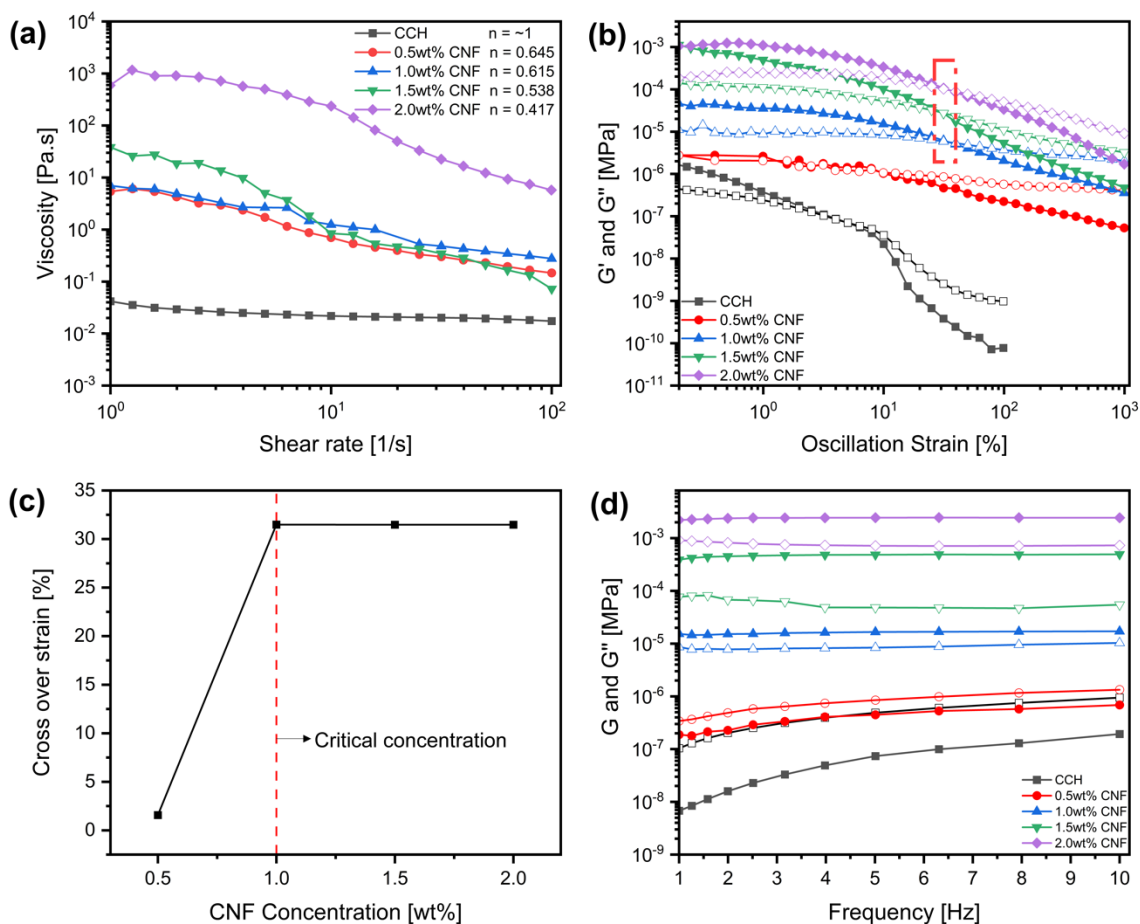
359 where  $\eta$  is the viscosity,  $\gamma$  is the strain rate,  $K$  is the flow consistency index, and  $n$  is the power-  
 360 law index.



361  
 362  
 363 *Figure 4. Microstructure characterization of additives and PCM composites (a) Pure CCH (b)*  
 364 *CNF (c) GNP (d) CCH-SC<sub>1.0</sub> (e) CCH-SCG<sub>1.0</sub> (f) CCH-SCG<sub>2.0</sub>. Visual observation of PCM*  
 365 *composites (g) freshly prepared sample (h) sample after 50 hours*

366  
 367 The higher viscosity values of the PCM composites at low strain rates are attributed to the increase  
 368 in the nanofibrils entanglement, which forms a network structure resisting the shearing of the  
 369 materials. These tangled networks, however, collapsed under a higher shear force when the shear  
 370 rate was continuously increased, resulting in a greater drop in viscosity. The shear thinning effect  
 371 is further associated with the thixotropic and pseudoplastic properties of CNF [23], which  
 372 becomes more pronounced with the increase in the concentration of CNF in the suspensions. The  
 373 power law index,  $n < 1$  further confirms the shear thinning behavior of the CNF-based composites,  
 374 and the reduction in the power law index with increased concentration of CNF signifies more  
 375 deviation from the Newtonian behavior ( $n=1$ ).

376 Storage ( $G'$ ) and loss modulus ( $G''$ ) measurements provide light on the form stability of the PCM  
 377 composites [46], which is essential since the material stability of PCMs is a key design feature  
 378 for certain thermal energy storage systems. In the amplitude sweep test shown in Figure 5b,  $G'$   
 379 and  $G''$  reflect the solid- and liquid-like behaviors, respectively.



380

381 *Figure 5. Rheology Characterization of CCH-based PCM mixtures: (a) Flow test, (b) Amplitude*  
 382 *sweep test, (c) Crossover strain as a function of CNF concentration, (d) Frequency sweep test.*  
 383 *Closed symbols in (b) and (d) represent storage modulus,  $G'$  while open symbols represent loss*  
 384 *modulus,  $G''$ .*

385 The cross-over strain is defined as the strain at which the material exhibits properties more typical  
 386 of a liquid than a solid ( $G'' > G'$ ). As seen in the amplitude sweep test in Figure 5b. The entangled  
 387 network of CNF causes the CCH/CNF composites to behave like solids, as shown by the  $G'$  values  
 388 being greater than the  $G''$  values for all CNF-containing samples. Due to an increase in CNF  
 389 interactions, the  $G'$  of CCH/CNF composites increased as the CNF concentration increased. The  
 390 strength of the CNF network may be measured by the cross-over strain, which is the transition  
 391 point beyond which  $G'' > G'$  (liquid-like behavior). The findings show that as the CNF  
 392 concentration increases from 0 wt% to 1 wt%, the cross-over strain increased linearly. Beyond this  
 393 point, the cross-over strain for CNF concentration of 1.5 wt% and 2 wt% did not increase beyond  
 394 31.5%, as seen in the marked area of Figure 5b and the plot in Figure 5c. This further shows that  
 395 1 wt% CNF is a critical concentration, enough to build robust entangled networks polymer-salt  
 396 system providing enhanced performance of the PCM composite.

397 Figure 5d demonstrates that in the frequency sweep of pure CCH and a sample with 0.5wt% CNF,  
 398 the loss modulus displays greater values than the storage modulus. This exemplifies a typical  
 399 characteristic of liquids. Also, the frequency-dependent rise in the  $G'$  and  $G''$  values of pure CCH

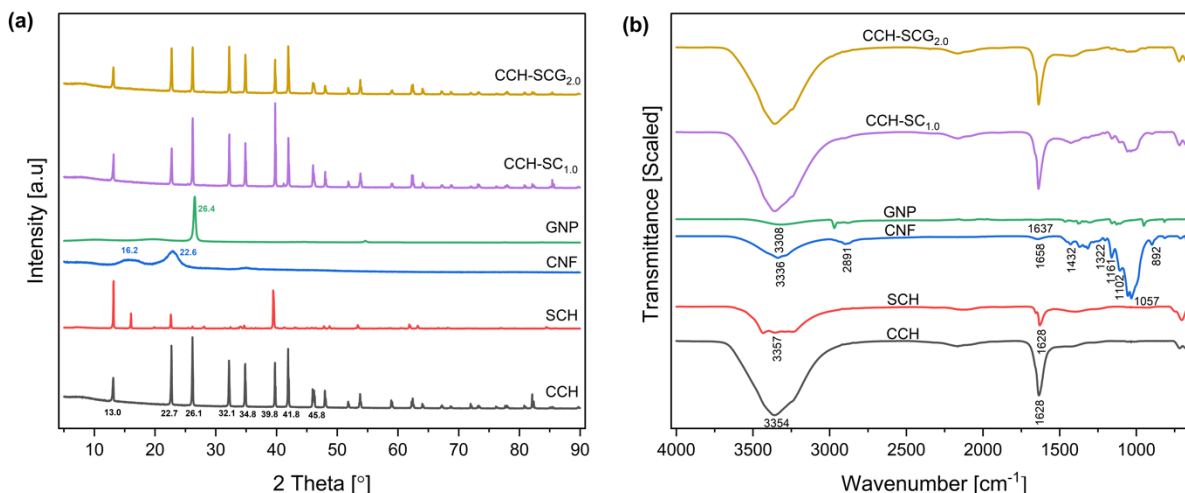
400 and sample with 0.5 wt% CNF is consistent with liquid-like relaxation characteristics in materials  
401 [46]. In contrast, the  $G'$  and  $G''$  values of samples with 1 wt%, 1.5 wt%, and 2 wt% CNF  
402 concentration did not show significant variation with frequency, indicating linear viscoelasticity  
403 in the samples. Moreover, the  $G'$  values are larger than the corresponding  $G''$  values for these mixes  
404 within the test frequency range, indicating solid-like characteristics. This further confirms that the  
405 formation of an adequate entangled network by CNF in the PCM matrix leads to a frequency  
406 independent response.

### 407 **3.5 Crystal Structure and Chemical Structure Characterization**

408 The XRD diffractograms of CCH, SCH, GNP, and other PCM composites were analyzed to  
409 generate insight into the crystalline structure stability and the interactions of hydrated salts in the  
410 composite as shown in Figure 6a. Standard X-ray diffraction powder patterns from the National  
411 Bureau of Standards' Institute of Material Research were used to compare the diffraction patterns  
412 of CCH with the reference data [47]. The XRD patterns strongly agree with the reference data with  
413 obvious peaks at  $13^\circ$ ,  $22.7^\circ$ ,  $26.1^\circ$ ,  $32.1^\circ$ ,  $34.8^\circ$ ,  $39.8^\circ$ ,  $41.8^\circ$ ,  $45.8^\circ$  which corresponds to (110),  
414 (210), (111), (211), (221), (330), (321) and (002) crystal plane respectively. Also, the  
415 diffractogram of SCH showed peak positions similar to CCH (but with lower intensity) at  $13^\circ$ ,  
416  $22.7^\circ$ ,  $26.1^\circ$ ,  $34.8^\circ$ , and  $39.8^\circ$ . This indicates that SCH and CCH have a similar crystal structure.  
417 The XRD plots and their match with relevant powder diffraction patterns are further reported in  
418 the supplementary information section. It is important to state that nucleation is governed by the  
419 close proximity of the crystal structure of the nucleator and hence, SCH can be safely used as  
420 nucleation triggering agent in CCH. While SCH is soluble completely soluble in CCH at an  
421 elevated temperature, it should be noted the temperature ranges of these experiments are in the  
422 range of  $13^\circ\text{C}$  to  $45.8^\circ\text{C}$  that we believe will not alter the nucleating properties of SCH. However,  
423 it should be noted that at very high temperatures and complex compositions, such as quaternary  
424 salt systems, the effect of SCH nucleator should be closely examined [48–51]. Furthermore, the  
425 XRD diffractogram of CNF showed a signature peak at  $16.2^\circ$  and  $22.6^\circ$ . These visible peaks are  
426 correlated to a cellulose type I structure, and they are located on the (110) and (200) crystal planes  
427 [52]. The (110) and (200) crystal planes also indicate the existence of both hydrophilic and  
428 hydrophobic regions in CNF [43]. The (002) crystal plane in carbon is responsible for the signature  
429 peak at  $26.4^\circ$  in GNP's diffraction pattern [53]. The diffraction pattern of the composite has the  
430 distinctive peaks of the constituent components without the introduction of additional peaks;  
431 therefore, this is suggestive of the physical mixing of the components without the generation of  
432 new compounds.

433 To further characterize the chemical structures of the PCM mixtures, FTIR measurement of the  
434 samples was conducted as shown in Figure 6b. For CCH, the characteristic peak at  $1628\text{ cm}^{-1}$  is  
435 attributed to the O-H stretching, and the broad peak at  $3354\text{ cm}^{-1}$  is ascribed to the hydroxyl  
436 stretching vibrations of water [10]. SCH also shows similar signature peaks to CCH, confirming  
437 the presence of hydroxyl functional group. For CNF, the peak at  $892\text{ cm}^{-1}$  indicates the glycosidic  
438 linkage in cellulose, while the signal at  $1057\text{ cm}^{-1}$  is caused by the C—O—C pyranose ring skeleton  
439 [54]. The signal at  $1102\text{ cm}^{-1}$  is due to the presence of glucose ring in cellulose, and the signal at  
440  $1161\text{ cm}^{-1}$  is due to asymmetric stretching in the C—O—C bond [55]. The maxima for CNF wagging  
441 symmetric bending and  $\text{CH}_2$  asymmetric bending are  $1432\text{ cm}^{-1}$  and  $1322\text{ cm}^{-1}$ , respectively. The  
442 peak at  $2891\text{ cm}^{-1}$  corresponds to the CH stretching vibration. The peaks at  $1667\text{ cm}^{-1}$  and  $3336$   
443  $\text{cm}^{-1}$  also indicate the stretching of water [56]. The FTIR spectra of the PCM composites show  
444 characteristic peaks corresponding to each component, confirming the XRD results that the

445 interaction between the components is not a chemical interaction since no new product is  
446 generated.  
447



448  
449 *Figure 6. Crystal Structure and Chemical Structure characterization of PCM mixtures: (a) XRD*  
450 *patterns of CCH-based PCM composites and their components, (b) FTIR spectra of CCH-based*  
451 *PCM composites and their components*

452

### 453 3.6 Thermal Cycling Stability Characterization of PCM Composites

454 A major metric to consider in the adoption of PCMs for long-term energy storage applications is  
455 thermal reliability after repeated thermal cycles. Figure 7 shows the thermal cycling stability of  
456 both pure CCH and the synthesized composites. Firstly, as can be shown in Figure 7a, the average  
457 energy storage capacity (ESC) of pure CCH is calculated to be  $177 \text{ Jg}^{-1}$  based on a preliminary  
458 thermal cycling measurement of up to 10 cycles using DSC analysis. This agrees with the values  
459 reported by Zhang et al.[18]. With the addition of CNF and SCH, the ESC of the resulting PCM  
460 composite, CCH-SC<sub>1,0</sub> is evaluated as  $181 \text{ Jg}^{-1}$ . The addition of GNP further increased the ESC of  
461 the composites. For instance, CCH-SCG<sub>1,0</sub> showed an ESC of  $185 \text{ Jg}^{-1}$ , and the ESC of CCH-  
462 SCG<sub>2,0</sub> is estimated to be  $182 \text{ Jg}^{-1}$ . When compared to the theoretical maximum ESC of CCH ( $190$   
463  $\text{Jg}^{-1}$ ), the ESC of maximum ESC of the composites,  $185.35 \text{ Jg}^{-1}$  represents 98% of the theoretical  
464 maximum, which is a notable increase when compared to that of CCH which reached 93% of the  
465 theoretical maximum ESC.

466 To evaluate the suitability of PCMs for industry-level application, larger quantities of test samples  
467 are required for testing in the laboratory environment. DSC test uses a smaller quantity of samples  
468 (10-15 mg), but this does not evaluate the supercooling degree effectively [21]. Hence, T-history  
469 measurements using a few grams of samples (15-20 g) were employed in the large-scale evaluation  
470 of the thermal cycling stability as shown in Figure 7b. After being subjected to 40 cycles, the ESC  
471 of pure CCH dropped from  $176 \text{ Jg}^{-1}$  to  $167 \text{ Jg}^{-1}$ . Also, there was a decline in the ESC of the  
472 composite samples during the first 10 cycles; this was ascribed to the initial interaction of the base  
473 materials, which led to effective dispersion and stability in the thermal cycling performance [57].  
474 CCH-SC<sub>1,0</sub> showed a stable ESC of  $178 \text{ Jg}^{-1}$  within 70 melt-freeze cycles. Furthermore, CCH-  
475 SCG<sub>1,0</sub> showed enhanced thermal performance with a stable ESC of  $184.3 \text{ Jg}^{-1}$  after 70 thermal

476 cycles, which is 97% stability when compared to the fifth cycle. The entangled network of CNF  
 477 reduced incongruent melting in CCH and increased GNP dispersion inside the PCM matrix based  
 478 on hydrophobic-hydrophobic interaction, improving thermal cycle stability. However, the CCH-  
 479 SCG<sub>2.0</sub> sample showed a lower ESC value of 178.4 Jg<sup>-1</sup> and 96% stability in ESC after 70 melt-  
 480 freeze cycles. This shows that increasing the dosage of GNP beyond a certain concentration limit  
 481 can lead to an increase in aggregation of the GNP in the PCM matrix which could limit the heat  
 482 transfer performance of the PCM composites.

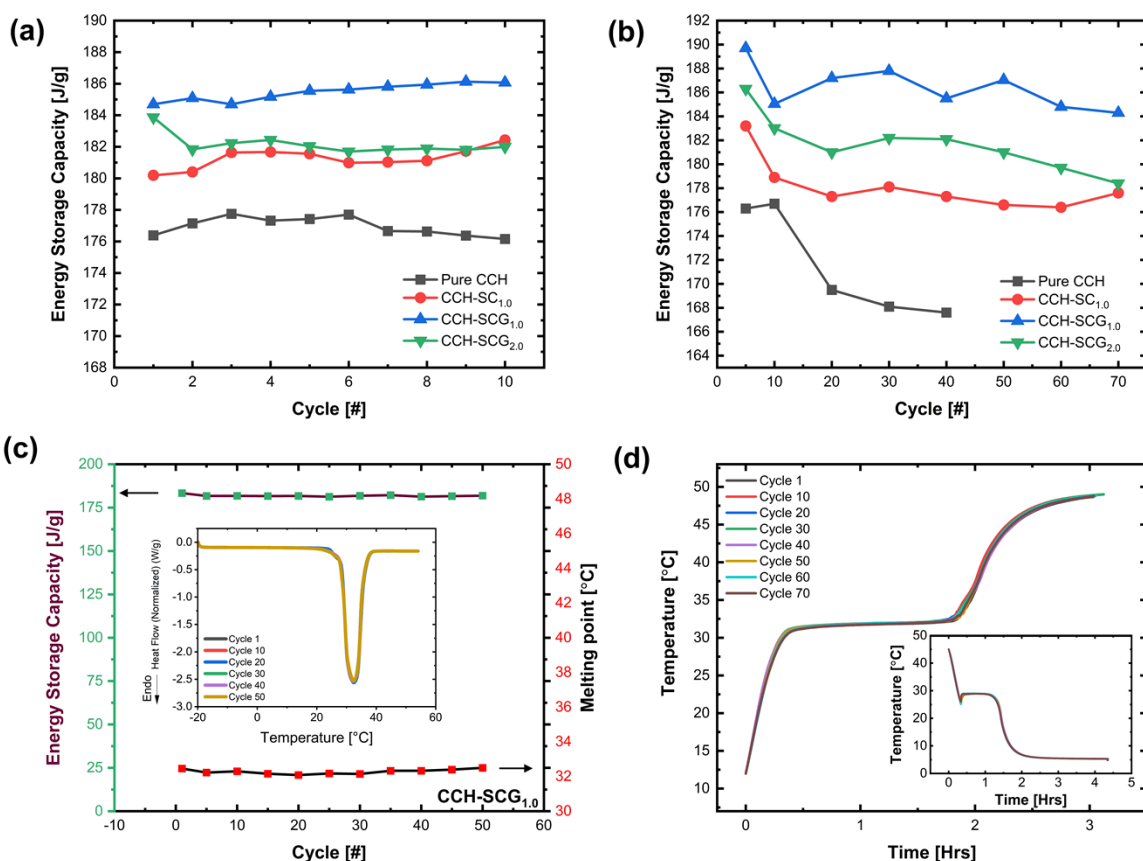
483 The thermal properties of the most stable composite, CCH-SCG<sub>1.0</sub> has further confirmed with the  
 484 DSC characterization over 50 cycles as reported in Figure 7c. The constant ESC value (181 Jg<sup>-1</sup>)  
 485 and overlapping of the DSC melting plots over 50 cycles (inset plot) proves the excellent thermal  
 486 stability of the material. Also, the T-history characterization results (Figure 7d) showed that the  
 487 melting and cooling curves of successive thermal cycles overlap well, confirming the thermal  
 488 stability of the materials. As the PCM composite was cooled to lower temperature regime, it  
 489 exhibited consistent freezing over repeated cycle with lower supercooling degree, The presence of  
 490 nucleator increased the nucleation sites thereby triggering crystallization in the PCM composite.  
 491 The consistent freezing of the PCM composite suggests the distribution of GNP by CNF material  
 492 was even and did not interfere with the crystallization of CCH. As reported in Table 3, the additives  
 493 further increased the melting point of pure CCH from 29.6 °C to 32 °C. The degree of supercooling  
 494 was lowered to ~ 3 °C due to the presence of nucleator, SCH. SCH reduced the interfacial energy  
 495 and enabled more nucleation sites in CCH, enhancing nucleation in the salt hydrate.

496  
497

498 Table 3. Thermal properties of pure Calcium Chloride Hexahydrate and its composite PCMs

Samples	Melting Enthalpy (DSC, Jg <sup>-1</sup> )	Melting temperature (DSC, °C)	Melting Enthalpy (T-history, Jg <sup>-1</sup> )	Melting temperature (T-history, °C)	Freezing temperature (T-history, °C)	Super-cooling degree (°C)
CCH	176.96	29.83	171.64	29.60	28.71	6.32
CCH-SC <sub>1.0</sub>	181.28	32.93	178.18	32.03	28.86	2.07
CCH-SCG <sub>1.0</sub>	185.35	32.63	186.42	32.12	28.88	2.99
CCH-SCG <sub>2.0</sub>	182.15	32.63	181.71	32.14	28.71	3.26

499  
500  
501

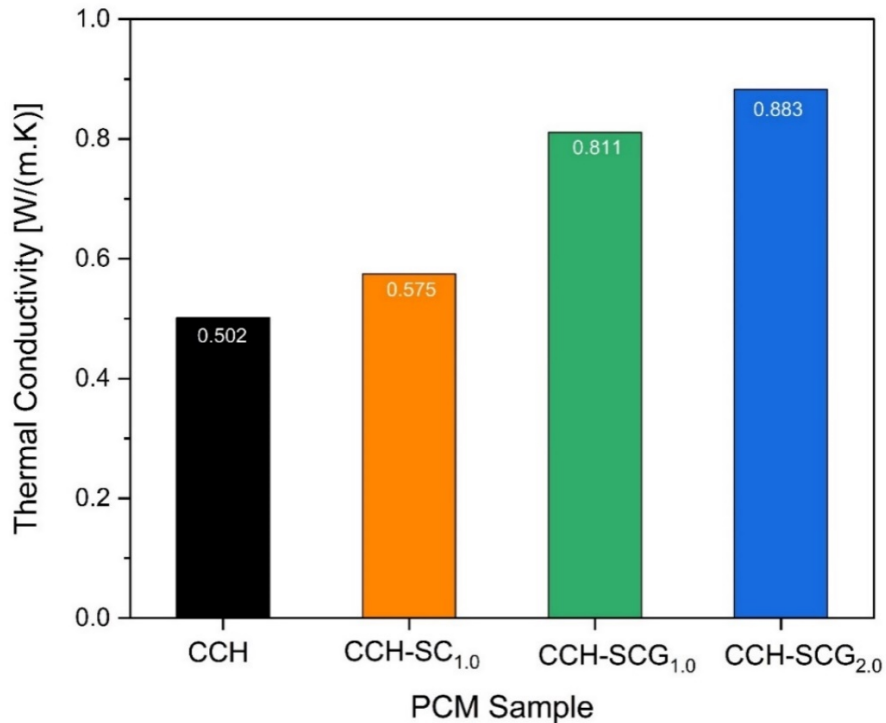


502  
 503 *Figure 7. Thermal cycling measurement of PCM mixtures (a) Energy storage capacity of PCM in*  
 504 *10 cycles using DSC; (b) Energy storage capacity of PCM in 70 cycles using T-History method;*  
 505 *(c) Line plot of energy storage capacity of CCH-SCG<sub>1,0</sub> in 50 cycles using DSC, inset shows the*  
 506 *overlay of the DSC thermograms over 50 cycles to show stability; (d) Heating and cooling (inset)*  
 507 *curve of CCH-SCG<sub>1,0</sub> in 70 cycles using T-History method.*

### 508 3.7 Thermal Conductivity Characterization of PCM Composites

509 Figure 8 displays the thermal conductivity measurement of CCH and the respective composites at  
 510 32 °C. It was observed that pure CCH had a thermal conductivity of 0.502 W/m-K. This value is  
 511 consistent with the thermal conductivity value of 0.546 W/m-K reported by Li et al. [16] and 0.529  
 512 W/m-K by Yuan et al. [42]. The thermal conductivity was slightly improved by adding 1 wt% CNF  
 513 and 3 wt% SCH, increasing it to 0.575 W/m-K. A further increase in thermal conductivity, to 0.811  
 514 W/m-K, was seen when 1 wt% GNP was added to the composite. The thermal conductivity value  
 515 of the composite was enhanced to 0.883 W/m-K with 2 wt% GNP, which is an increase of 76%  
 516 compared to the thermal conductivity of pure CCH. This study confirms that graphitic materials,  
 517 such as GNP, improve the thermal conductivity values of CCH leading to a corresponding  
 518 improvement in charging and discharging rate of the PCMs in TES applications. GNP  
 519 nanomaterial acts as the high thermal conductivity medium for the PCM composites, and its higher  
 520 heat transfer ability is responsible for the increase in the composites' thermal conductivity values.  
 521 Although increased heat-transfer characteristics were observed in the produced PCM composite,

522 the added 2 wt% concentration of GNP may not be sufficient to deliver relatively high thermal  
 523 conductivity. In the study by Yang et al. [58], the thermal conductivity of the PCM after adding  
 524 5.3% GNP was reported to be 1.35 W/m-K. The major issues with the extra addition of GNP  
 525 include increased materials cost and higher potential for GNP aggregation that can reduce the  
 526 performance of the PCM composites. Therefore, the concentration ranges of carbon materials for  
 527 thermal conductivity enhancement should be reconsidered in designing high-performance PCM  
 528 composites [24].  
 529



530  
 531 *Figure 8. Thermal conductivity of CCH and CCH-based PCM composites at 32 °C: the influence of GNP*  
 532 *concentrations*

533 **4 Conclusions**

534 In this study, PCM composites with enhanced thermal characteristics for application in buildings  
 535 system were developed by combining CaCl<sub>2</sub>.6H<sub>2</sub>O with cellulose nanofibril, which serves as a  
 536 thickening and dispersing agent; graphene nanoplatelet, used to enhance the thermal conductivity;  
 537 and SrCl<sub>2</sub>.6H<sub>2</sub>O, which is a nucleating agent for CCH. With the addition of 3 wt% of SrCl<sub>2</sub>.6H<sub>2</sub>O,  
 538 the degree of supercooling was significantly reduced to 3 °C. The utilization of 1 wt% of  
 539 environmentally friendly and thermally stable CNF in the composite exhibited an effective  
 540 mechanism in dispersing GNP throughout the PCM composites, thereby forming a compact  
 541 structure. CNF has relatively lower cost compared to other thickeners and polymers since it is an  
 542 abundant organic polymer, which helps to keep the overall cost of PCM composite lower compared  
 543 to other composites in the literature. Also, 1% concentration of CNF is needed to maintain high  
 544 latent heat capacity, as compared to other composites losing >5-10% of their capacity with the  
 545 addition of thickening agents. Structural characterization results confirm the physical mixing of  
 546 the constituent materials in the PCM composites. Using T-history measurement, the resulting PCM

547 composites including GNP predispersed with CNF demonstrated high latent heat energy of 186  
548 Jg<sup>-1</sup>, melting temperature of 32 °C, supercooling of 3 °C and excellent thermal stability after 70  
549 successive melt-freeze cycles. The produced PCM composites exhibited a maximum thermal  
550 conductivity of 0.883 W/m-K, 76% higher than that of pure CCH. The enhancement mechanism  
551 in these PCM composites is based on the entangled structure and amphiphilicity of CNF, which  
552 allow it to make hydrophobic contact with GNP, resulting in a greater dispersion of GNP  
553 throughout the composite system. Moreover, CNF is able to inhibit incongruent melting of CCH  
554 by inducing hydrogen bonding in the system, which regulates the release of water required for  
555 crystallization. This produces a salt hydrate PCM composite with enhanced thermal energy storage  
556 characteristics. This study sheds light on the potential use of environmentally friendly natural  
557 polymers like CNF in the rapidly developing area of thermal energy storage, especially in building  
558 systems.

## 559 **Nomenclature**

560	CCH	Calcium chloride hexahydrate
561	CNF	Cellulose nanofiber
562	CNT	Carbon nanotube
563	DSC	Differential scanning calorimetry
564	EG	Expanded graphite
565	ESC	Energy storage capacity
566	FTIR	Fourier transform infrared spectroscopy
567	GNP	Graphene nanoplatelets
568	GO	Graphene oxide
569	LHTESS	latent heat thermal energy storage systems
570	PCM	Phase change materials
571	SCH	Strontium chloride hexahydrate
572	SEM	Scanning electron microscopy
573	TES	Thermal energy storage
574	XRD	X-ray diffraction

575

## 576 **Parameters**

577	$\Delta H$	phase change enthalpy
578	$T_m$	melting temperature
579	$T_f$	freezing temperature
580	$T_n$	onset of nucleation temperature
581	$\Delta T$	supercooling degree (°C)

## 582 **Acknowledgments**

583 This work was sponsored by the U. S. Department of Energy's Building Technologies Office under  
584 Contract No. DE-AC05-00OR22725 with UT-Battelle, LLC. The authors would like to  
585 acknowledge Mr. Sven Mumme, Technology Manager – Building Envelope, U.S. Department of  
586 Energy Building Technologies Office.

587 **Declaration of competing interest**

588 The authors state that they have no known conflicting financial interests or personal ties that may  
589 be seen as having influenced the work described in this study.

590

591 **CRedit author statement**

592 **Damilola O Akamo:** Conceptualization, Methodology, Investigation, Data curation, Formal  
593 analysis, Writing – original draft. **Kai Li:** Investigation, Validation, Resources, Writing – Review  
594 and Editing. **Tugba Turnaoglu:** Validation, Formal analysis, Writing – Review and Editing.  
595 **Navin Kumar:** Conceptualization, Resources, Writing – Review and Editing. **Yuzhan Li:**  
596 Conceptualization, Resources, Writing – Review and Editing. **Collin Pekol:** Resources,  
597 Investigation, Writing – Review and Editing. **Nitish Bibhanshu:** Resources, Visualization,  
598 Software, Writing – Review and Editing. **Jason Hirschey:** Resources, Writing – Review and  
599 Editing. **Tim LaClair:** Funding acquisition, Project Administration, Writing – Review and  
600 Editing. **Monojoy Goswami:** Resources, Writing – Review and Editing, **David J. Keffer:**  
601 Supervision, Writing – Review and Editing. **Orlando Rios:** Conceptualization, Methodology,  
602 Supervision. **Kyle R. Gluesenkamp:** Conceptualization, Funding acquisition, Project  
603 Administration, Supervision, Writing – Review and Editing

604 **References**

- 605 1. Nazir H, Batool M, Bolivar Osorio FJ, Isaza-Ruiz M, Xu X, Vignarooban K, Phelan P, Inamuddin,  
606 Kannan AM. Recent developments in phase change materials for energy storage applications: A  
607 review. *Int J Heat Mass Transf.* 2019;129:491–523.
- 608 2. Sikiru S, Oladosu TL, Amosa TI, Kolawole SY, Soleimani H. Recent advances and impact of phase  
609 change materials on solar energy: A comprehensive review. *J Energy Storage.* 2022 Sep 1;53.
- 610 3. Kumar N, Hirschey J, LaClair TJ, Gluesenkamp KR, Graham S. Review of stability and thermal  
611 conductivity enhancements for salt hydrates. *J Energy Storage.* 2019 Aug;24:100794.
- 612 4. Li X, Zhou Y, Nian H, Zhang X, Dong O, Ren X, Zeng J, Hai C, Shen Y. Advanced Nanocomposite  
613 Phase Change Material Based on Calcium Chloride Hexahydrate with Aluminum Oxide  
614 Nanoparticles for Thermal Energy Storage. *Energy and Fuels.* 2017;31(6):6560–7.
- 615 5. Zou T, Fu W, Liang X, Wang S, Gao X, Zhang Z, Fang Y. Preparation and performance of modified  
616 calcium chloride hexahydrate composite phase change material for air-conditioning cold storage.  
617 *International Journal of Refrigeration.* 2018;95:175–81.
- 618 6. Al-harashsheh M, Abu-Arabi M, Mousa H, Alzghoul Z. Solar desalination using solar still enhanced  
619 by external solar collector and PCM. *Appl Therm Eng.* 2018 Jan 5;128:1030–40.
- 620 7. Kalapala L, Devanuri JK. Influence of operational and design parameters on the performance of a  
621 PCM based heat exchanger for thermal energy storage – A review. *J Energy Storage.* 2018 Dec  
622 1;20:497–519.
- 623 8. Faraj K, Khaled M, Faraj J, Hachem F, Castelain C. Phase change material thermal energy storage  
624 systems for cooling applications in buildings: A review. *Renewable and Sustainable Energy*  
625 *Reviews.* 2020 Mar 1;119.
- 626 9. Hirschey JR, Kumar N, Gluesenkamp KR, Graham S, Hirschey J, Robert ;, Kumar N;, Turnaoglu  
627 T;, Gluesenkamp KR;, Samuel G, Turnaoglu T. Review of Low-Cost Organic and Inorganic Phase

- 628 Change Materials with Phase Change Temperature between 0°C and 65°C. International High  
629 Performance Buildings Conference. 2021;10.
- 630 10. Li X, Zhou Y, Nian H, Ren X, Dong O, Hai C, Shen Y, Zeng J. Phase change behavior of latent  
631 heat storage media based on calcium chloride hexahydrate composites containing strontium chloride  
632 hexahydrate and oxidation expandable graphite. *Appl Therm Eng.* 2016;102:38–44.
- 633 11. Akamo DO, Kumar N, Li Y, Pekol C, Li K, Goswami M, Hirschey J, LaClair TJ, Keffer DJ, Rios  
634 O, Gluesenkamp KR. Stabilization of low-cost phase change materials for thermal energy storage  
635 applications. *iScience.* 2023 Jul;26(7):107175.
- 636 12. Xie N, Huang Z, Luo Z, Gao X, Fang Y, Zhang Z. Inorganic Salt Hydrate for Thermal Energy  
637 Storage. *Applied Sciences* 2017, Vol 7, Page 1317. 2017 Dec 18;7(12):1317.
- 638 13. Xu X, Dong Z, Memon SA, Bao X, Cui H. Preparation and Supercooling Modification of Salt  
639 Hydrate Phase Change Materials Based on CaCl<sub>2</sub>·2H<sub>2</sub>O/CaCl<sub>2</sub>. *Materials* 2017, Vol 10, Page 691.  
640 2017 Jun 23;10(7):691.
- 641 14. Xu X, Dong Z, Memon SA, Bao X, Cui H. Preparation and supercooling modification of salt hydrate  
642 phase change materials based on CaCl<sub>2</sub>·2H<sub>2</sub>O/CaCl<sub>2</sub>. *Materials.* 2017;10(7).
- 643 15. Zhang X, Li X, Zhou Y, Hai C, Shen Y, Ren X, Zeng J. Calcium Chloride  
644 Hexahydrate/Diatomite/Paraffin as Composite Shape-Stabilized Phase-Change Material for  
645 Thermal Energy Storage. *Energy and Fuels.* 2018;32(1):916–21.
- 646 16. Li C, Li M, Li Y. Tailored calcium chloride hexahydrate as a composite phase change material for  
647 cold storage. *J Energy Storage.* 2022;56(July).
- 648 17. Thakkar J, Bowen N, Chang AC, Horwath P, Sobkowicz MJ, Kośny J. Optimization of Preparation  
649 Method, Nucleating Agent, and Stabilizers for Synthesizing Calcium Chloride Hexahydrate  
650 (CaCl<sub>2</sub>·6H<sub>2</sub>O) Phase Change Material. *Buildings.* 2022;12(10).
- 651 18. Zhang Q, Ma F, Tan W, Liu L, Jing M, Sun T. Enhanced heat storage performance of CaCl<sub>2</sub>·6H<sub>2</sub>O  
652 using BN nanosheet as an additive. *Heat and Mass Transfer/Waerme- und Stoffuebertragung.*  
653 2022;(0123456789).
- 654 19. Xu X, Cui H, Memon SA, Yang H, Tang W. Development of novel composite PCM for thermal  
655 energy storage using CaCl<sub>2</sub>·6H<sub>2</sub>O with graphene oxide and SrCl<sub>2</sub>·6H<sub>2</sub>O. *Energy Build.*  
656 2017;156:163–72.
- 657 20. Li MC, Wu Q, Song K, Lee S, Qing Y, Wu Y. Cellulose Nanoparticles:  
658 Structure–Morphology–Rheology Relationships. 2015 [cited 2023 Mar 18]; Available from:  
659 <https://pubs.acs.org/sharingguidelines>
- 660 21. Xu X, Liu F, Jiang L, Zhu JY, Haagensohn D, Wiesenborn DP. Cellulose Nanocrystals vs. Cellulose  
661 Nanofibrils: A Comparative Study on Their Microstructures and Effects as Polymer Reinforcing  
662 Agents. 2013 [cited 2022 Jul 7]; Available from: [www.acsami.org](http://www.acsami.org)
- 663 22. Oh K, Kwon S, Xu W, Wang X, Toivakka M. Effect of micro- and nanofibrillated cellulose on the  
664 phase stability of sodium sulfate decahydrate based phase change material. *Cellulose.*  
665 2020;27(9):5003–16.
- 666 23. Li M chun, Wu Q, Song K, Lee S, Qing Y, Wu Y. Cellulose Nanoparticles: Structure – Morphology  
667 – Rheology Relationships. 2015;
- 668 24. Shen Z, Kwon S, Lee HL, Toivakka M, Oh K. Enhanced thermal energy storage performance of salt  
669 hydrate phase change material: Effect of cellulose nanofibril and graphene nanoplatelet. *Solar*  
670 *Energy Materials and Solar Cells.* 2021 Jun;225(February):111028.
- 671 25. Naghdbishi A, Yazdi ME, Akbari G. Experimental investigation of the effect of multi-wall carbon  
672 nanotube – Water/glycol based nanofluids on a PVT system integrated with PCM-covered collector.  
673 *Appl Therm Eng.* 2020 Sep 1;178.
- 674 26. Huang K, Li J, Luan X, Liu L, Yang Z, Wang C. Effect of Graphene Oxide on Phase Change  
675 Materials Based on Disodium Hydrogen Phosphate Dodecahydrate for Thermal Storage. *ACS*  
676 *Omega.* 2020;5(25):15210–7.

- 677 27. Zou T, Fu W, Liang X, Wang S, Gao X, Zhang Z, Fang Y. Hydrophilic modification of expanded  
678 graphite to develop form-stable composite phase change material based on modified  $\text{CaCl}_2 \cdot 6\text{H}_2\text{O}$ .  
679 Energy. 2020 Jan 1;190.
- 680 28. Cui H, Wang P, Yang H, Xu T. Design and preparation of salt hydrate/ graphene oxide@ $\text{SiO}_2$ / SiC  
681 composites for efficient solar thermal utilization. Solar Energy Materials and Solar Cells. 2022 Mar  
682 1;236.
- 683 29. Hirschey J, Goswami M, Akamo DO, Kumar N, Li Y, LaClair TJ, Gluesenkamp KR, Graham S.  
684 Effect of expanded graphite on the thermal conductivity of sodium sulfate decahydrate  
685 ( $\text{Na}_2\text{SO}_4 \cdot 10\text{H}_2\text{O}$ ) phase change composites. J Energy Storage [Internet]. 2022  
686 Aug;52(PB):104949. Available from: <https://doi.org/10.1016/j.est.2022.104949>
- 687 30. Goswami M, Kumar N, Li Y, Rios O, Akamo DO, Hirschey J, LaClair TJ, Gluesenkamp KR.  
688 Comparison of water nanodroplet properties on different graphite-based substrates. AIP Adv  
689 [Internet]. 2021 Mar 1;11(3):035009. Available from: <https://doi.org/10.1063/5.0042414>
- 690 31. Yang W, Gong Y, Zhao X, Liu T, Zhang Y, Chen F, Fu Q. Strong and Highly Conductive Graphene  
691 Composite Film Based on the Nanocellulose-Assisted Dispersion of Expanded Graphite and  
692 Incorporation of Poly(ethylene oxide). ACS Sustain Chem Eng. 2019;7(5):5045–56.
- 693 32. Xu S, Yu W, Jing M, Huang R, Zhang Q, Fu Q. Largely Enhanced Stretching Sensitivity of  
694 Polyurethane/Carbon Nanotube Nanocomposites via Incorporation of Cellulose Nanofiber. Journal  
695 of Physical Chemistry C. 2017;121(4):2108–17.
- 696 33. Xu S, Yu W, Yao X, Zhang Q, Fu Q. Nanocellulose-assisted dispersion of graphene to fabricate  
697 poly(vinyl alcohol)/graphene nanocomposite for humidity sensing. Compos Sci Technol. 2016 Aug  
698 2;131:67–76.
- 699 34. Kumar N, Banerjee D. Characterization of Phase Change Materials (PCM) using T-History method.  
700 2016;
- 701 35. Goswami M, Kumar N, Li Y, Hirschey J, LaClair TJ, Akamo DO, Sultan S, Rios O, Gluesenkamp  
702 KR, Graham S. Understanding supercooling mechanism in sodium sulfate decahydrate phase-  
703 change material. J Appl Phys. 2021;129(24).
- 704 36. Gustafsson SE. Transient plane source techniques for thermal conductivity and thermal diffusivity  
705 measurements of solid materials. Review of Scientific Instruments. 1991;62(3):797–804.
- 706 37. Qian D, Fang D, Xu Y. You may also like In-situ growth of high-density ultrafine Ag 3 PO 4  
707 nanoparticles on 3D  $\text{TiO}_2$  hierarchical spheres for enhanced photocatalytic degradation of organic  
708 pollutants. J Phys D Appl Phys.
- 709 38. ISO - ISO 22007-2:2022 - Plastics — Determination of thermal conductivity and thermal diffusivity  
710 — Part 2: Transient plane heat source (hot disc) method [Internet]. [cited 2023 Mar 20]. Available  
711 from: <https://www.iso.org/standard/81836.html>
- 712 39. Feilchenfeld H, Sarig S. Calcium Chloride Hexahydrate: A Phase-Changing Material for Energy  
713 Storage. Industrial and Engineering Chemistry Product Research and Development.  
714 1985;24(1):130–3.
- 715 40. Tortello M, Colonna S, Bernal M, Gomez J, Pavese M, Novara C, Giorgis F, Maggio M, Guerra G,  
716 Saracco G, Gonnelli RS, Fina A. Effect of thermal annealing on the heat transfer properties of  
717 reduced graphite oxide flakes: A nanoscale characterization via scanning thermal microscopy.  
718 Carbon N Y. 2016 Nov 1;109:390–401.
- 719 41. Xu S, Yu W, Yao X, Zhang Q, Fu Q. Nanocellulose-assisted dispersion of graphene to fabricate  
720 poly(vinyl alcohol)/graphene nanocomposite for humidity sensing. Compos Sci Technol.  
721 2016;131:67–76.
- 722 42. Yuan K, Zhou Y, Sun W, Fang X, Zhang Z. A polymer-coated calcium chloride  
723 hexahydrate/expanded graphite composite phase change material with enhanced thermal reliability  
724 and good applicability. Compos Sci Technol. 2018 Mar 1;156:78–86.
- 725 43. Oh K, Shen Z, Kwon S, Toivakka M. Thermal properties of graphite/salt hydrate phase change  
726 material stabilized by nanofibrillated cellulose. Cellulose. 2021;28(11):6845–56.

- 727 44. Li Y, Zhu H, Shen F, Wan J, Lacey S, Fang Z, Dai H, Hu L. Nanocellulose as green dispersant for  
728 two-dimensional energy materials. *Nano Energy*. 2015;13:346–54.
- 729 45. Koponen AI. The effect of consistency on the shear rheology of aqueous suspensions of cellulose  
730 micro- and nanofibrils: a review. *Cellulose*. 2020;27(4):1879–97.
- 731 46. Qi GQ, Liang CL, Bao RY, Liu ZY, Yang W, Xie BH, Yang MB. Polyethylene glycol based shape-  
732 stabilized phase change material for thermal energy storage with ultra-low content of graphene  
733 oxide. *Solar Energy Materials and Solar Cells*. 2014;123:171–7.
- 734 47. Morris MC, McMurdie HF, Evans EH, Paretzkin B, Parker HS, Pyrros NP, Hubbard CR. Standard  
735 X-Ray Diffraction Powder Patterns. NBS Monograph (United States). US Department of  
736 Commerce, National Bureau of Standards; 1982.
- 737 48. Han H, Ji X, Ma J, Xu Z, Guo L, Li D, Yao Y. Water Activity, Solubility Determination, and Model  
738 Simulation of the CaCl<sub>2</sub>-SrCl<sub>2</sub>-H<sub>2</sub>O Ternary System at 323.15 K. *J Chem Eng Data* [Internet]. 2018  
739 May 10 [cited 2023 Oct 11];63(5):1636–41. Available from: <https://pubs.acs.org/sharingguidelines>
- 740 49. Gao YY, Ye C, Zhang WY, Yang L, Sang SH, Huang Y. Phase Equilibria in the Ternary System  
741 CaCl<sub>2</sub>-SrCl<sub>2</sub>-H<sub>2</sub>O and the Quaternary System KCl-CaCl<sub>2</sub>-SrCl<sub>2</sub>-H<sub>2</sub>O at 373 K. *J Chem Eng Data*  
742 [Internet]. 2018 Aug 9 [cited 2023 Oct 11];63(8):2738–42. Available from:  
743 <https://pubs.acs.org/sharingguidelines>
- 744 50. Li D, Zhang Z, Fan R, Yang S. Solid-Liquid Phase Equilibria in the Aqueous Systems (CaCl<sub>2</sub> +  
745 SrCl<sub>2</sub> + H<sub>2</sub>O) and (NaCl + CaCl<sub>2</sub> + SrCl<sub>2</sub> + H<sub>2</sub>O) at 288.15 K. *J Chem Eng Data* [Internet]. 2019  
746 Jun 13 [cited 2023 Oct 11];64(6):2767–73. Available from: <https://pubs.acs.org/sharingguidelines>
- 747 51. Li D, Shi T, Zhao H, Li C, Gu S. Phase Equilibria in the Quaternary Systems (KCl + CaCl<sub>2</sub> + SrCl<sub>2</sub> +  
748 H<sub>2</sub>O) and (LiCl + NaCl + SrCl<sub>2</sub> + H<sub>2</sub>O) at 288.15 K and 0.1 MPa. *J Chem Eng Data* [Internet]. 2020  
749 Nov 12 [cited 2023 Oct 11];65(11):5266–74. Available from:  
750 <https://dx.doi.org/10.1021/acs.jced.0c00435>
- 751 52. He W, Jiang S, Zhang Q, Pan M. Isolation and characterization of cellulose nanofibers from  
752 *Bambusa rigida*. *Bioresources*. 2013;8(4):5678–89.
- 753 53. Kumar N, Srivastava VC. Simple Synthesis of Large Graphene Oxide Sheets via Electrochemical  
754 Method Coupled with Oxidation Process. *ACS Omega*. 2018;3(8):10233–42.
- 755 54. Rani A, Monga S, Bansal M, Sharma A. Bionanocomposites reinforced with cellulose nanofibers  
756 derived from sugarcane bagasse. *Polym Compos*. 2018;39:E55–64.
- 757 55. Ventura-Cruz S, Tecante A. Extraction and characterization of cellulose nanofibers from Rose stems  
758 (*Rosa spp.*). *Carbohydr Polym*. 2019;220(May):53–9.
- 759 56. Khatri Z, Arain RA, Jatoi AW, Mayakrishnan G, Wei K, Kim IS. Dyeing and characterization of  
760 cellulose nanofibers to improve color yields by dual padding method. *Cellulose*. 2013;20(3):1469–  
761 76.
- 762 57. Li Y, Kumar N, Hirsche J, Akamo DO, Li K, Tugba T, Goswami M, Orlando R, LaClair TJ,  
763 Graham S, Gluesenkamp KR. Stable salt hydrate-based thermal energy storage materials. *Compos*  
764 *B Eng* [Internet]. 2022 Mar;233(January):109621. Available from:  
765 <https://linkinghub.elsevier.com/retrieve/pii/S1359836822000117>
- 766 58. Yang J, Zhang E, Li X, Zhang Y, Qu J, Yu ZZ. Cellulose/graphene aerogel supported phase change  
767 composites with high thermal conductivity and good shape stability for thermal energy storage.  
768 *Carbon N Y*. 2016 Mar 1;98:50–7.
- 769